THE JOURNAL OF PHYSICAL CHEMISTRY C

Article

Cite This: J. Phys. Chem. C 2019, 123, 25437−25447

pubs.acs.org/JPCC

Maximizing Thermoelectric Figures of Merit by Uniaxially Straining Indium Selenide

Leonard W. Sprague Jr.,[†] Cancan Huang,[†] Jeong-Pil Song,*[,†,‡] and Brenda M. Rubenstein[†]

[†]Department of Chemistry, Brown University, Providence, Rhode Island 02912, United States

[‡]Department of Physics, University of Arizona, Tucson, Arizona 85721, United States

Supporting Information

ABSTRACT: A majority of the electricity currently generated is regrettably lost as heat. Engineering high-efficiency thermoelectric materials which can convert waste heat back into electricity is therefore vital for reducing our energy fingerprint. ZT, a dimensionless figure of merit, acts as a beacon of promising thermoelectric materials. However, engineering materials with large ZT values is practically challenging, since maximizing ZT requires optimizing many interdependent material properties. Motivated by recent studies on bulk indium selenide that suggest it may have favorable thermoelectric properties, here we present the thermoelectric properties of monolayer indium selenide in the presence of uniaxial strain using first-principles calculations conjoined with semiclassical Boltzmann transport theory. Our calculations indicate that conduction band convergence occurs at a compressive strain of −6% along the zigzag direction and results in an enhancement of ZT for p-type indium selenide at room temperature. Further enhancements occur at −7% as the valence bands similarly converge, reaching a maximum ZT value of 0.46, which is one of the largest monolayer InSe figures of merit recorded to date at room temperature. The importance of strain is directly reflected by the enhanced transport coefficients observed at strains nearing those which give rise to the band degeneracies we observe. Our studies demonstrate that strain-induced transitions can play a key role in the engineering of promising thermoelectric materials.

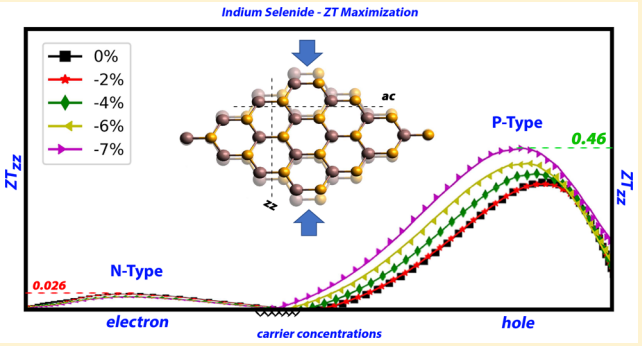

INTRODUCTION

Thermoelectric materials, those that convert heat into electricity, have been intensely studied in recent decades with the aim of improving the cooling and power generation efficiency of electronic equipment.[1−4] Solar energy devices, for example, are only able to generate electricity in response to the 50−60% of the sun's radiation that lies within the visible and ultraviolet portions of the spectrum using conventional semiconductor-based systems; thermoelectric devices, meanwhile, are able to convert much of the remaining 40−50% of radiation, largely infrared, into electricity.[2] Coupling of photovoltaic and thermoelectric devices would therefore vastly increase the range of accessible solar radiation for energy conversion. Regular assessments of national energy generation, consumption, and waste further demonstrate thermoelectric devices' practicality and importance, as over 60% of generated electricity is "rejected" as waste heat.[1,5]

The performance of thermoelectric materials is governed by the dimensionless figure of merit defined as

$$\mathrm{ZT} = \frac{S^2\sigma T}{\kappa_e + \kappa_{ph}} \quad (1)$$

where S is the thermoelectric power (Seebeck coefficient), T is the absolute temperature, σ is the electrical conductivity, and κ_e (κ_{ph}) is the electronic (lattice) thermal conductivity.[1,2,6−8] ZT is the pivotal parameter in determining the efficiency, η, of a thermoelectric device:

$$\eta = \frac{(T_{hot} - T_{cold})}{T_{hot}} \frac{\sqrt{1 + \mathrm{ZT}_{av}} - 1}{\sqrt{1 + \mathrm{ZT}_{av}} - \frac{T_{cold}}{T_{hot}}} \quad (2)$$

ZT_{av} is the average value of ZT across reservoir temperatures and carrier concentration (holes and electrons) and T_c and T_h are the temperatures of the cold and hot reservoirs.[1,2,6−8] Maximizing the efficiency of a thermoelectric "engine" therefore requires maximizing ZT. For instance, a thermoelectric power conversion device with a ZT_{av} of 3 operating between 300 and 800 K, would operate at about 60% of the Carnot efficiency. At present, many thermoelectric devices for room-temperature applications are still struggling to reach even this efficiency. Engineering novel materials that improve upon ZT at favorable operating temperatures is thus necessary to

Received: June 14, 2019
Revised: September 9, 2019
Published: October 8, 2019

DOI: 10.1021/acs.jpcc.9b05681
J. Phys. Chem. C 2019, 123, 25437−25447

reach a level of efficiency worthwhile for global scale energy applications.

Engineering thermoelectrics, however, holds a crucial caveat: optimization of three interdependent parameters in the figure of merit, which is a nontrivial task. Due to this, identifying structural and electronic characteristics of materials that promote larger values of ZT is fundamentally challenging. Material exploration therefore tends to involve individual adjustments to geometry and/or electronic band structure (via stress, doping, etc.), in the hopes of finding larger S or σ and smaller κ; band degeneracies and flexible lattice structures are signatures of potentially high ZT materials.

When optimizing the ZT parameters of a material, another important factor must be considered: semiconductor character, or the type (and size) of the material's band gap. Band gaps are required to allow for "engine" action as a thermoelectric device, demonstrated by current practical thermoelectric materials almost invariably being semiconductors.[9] Zero band gap (conductor) systems and large band gap (insulating) systems are therefore intrinsically disadvantaged as work engines for thermoelectric energy conversion.[1] Reducing the dimensionality of non-semi-conducting bulk systems, however, does open up their possible use; *ab initio* work on leading 2D materials and their bulk (3D) counterparts demonstrates that band gaps typically increase as the number of layers in 3D is decreased towards the monolayer limit.[10,11]

Strides in material expeditions for better ZT have begun to bear fruit; bismuth telluride (Bi_2Te_3) and its alloys (e.g., BiSbTe),[12−18] lead telluride (PbTe),[19−21] and tin selenide (SnSe)[22,23] have recently been identified as high ZT materials whose figures of merit exceed the previous ZT barrier of unity.[19] These materials' impressively large ZT_{max} values of 1.6 (alloys: 1.4−1.8), 2.2, and 2.6, respectively, were attained by reducing thermal conductivity values, primarily by leveraging materials with inherently small κ's. Nevertheless, these materials (excluding Bi_2Te_3 and some alloys) often achieve their highest ZT values at high T (>700 K) and incorporate environmentally unfriendly and toxic heavy elements.[22,24,25] Current thermoelectric material prospects are therefore in dire need of enhanced room-temperature ZTs to satisfy commercial need.

In the quest for higher ZT values, attention has recently turned to low-dimensional materials. For instance, in bismuth-telluride alloys, thermal conductivity was reduced via nanostructuring[26−28] to engineer larger ZT values. However, certain restrictions appear with reduced dimensionality in thermoelectric applications. Although inclusion of nanostructures reduces thermal conductivity in bulk alloys, the quantum confinement of 2D systems often instead results in an increased thermal conductivity over bulk (3D),[16,29−31] thus making it seem like the most likely outcome is for 2D materials to have *lower* ZT values than their 3D counterparts.

In spite of this, one of the most promising aspects of 2D materials is their tunability via chemical modification (doping/defects), strain, and stacking, which enables the engineering of semiconductor and thermoelectric features (e.g., desirable band gaps or high electron mobility).[32−34] Furthermore, some 2D structures exhibit large band gaps or increased carrier mobilities, which may overall magnify their ZT values. One way of inducing such effects is by applying a strain. For instance, 2D layered phosphorene under tensile strain was found to be an indirect, medium band gap semiconductor exhibiting large ZT values and therefore a promising potential thermoelectric material.[35,36] Groups III and IV post-transition metal chalcogenides have also garnered attention because of their semiconducting character. In particular, recent work has focused on electronic/photonic properties and tunability of gallium and indium sulfide/selenide systems and related alloys.[37−48]

One transition metal chalcogenide ripe for engineering improved ZT values is indium selenide. 3D InSe exhibits a ZT of 1.48 at 705 K in large part due to its exceptionally low lattice thermal conductivity ($\kappa_{ph} \sim 0.74$ W m^{-1} K^{-1}).[49,50] Motivated by improvements to ZT realized in other materials by reducing dimensionality, few-layer InSe was recently synthesized and was found to possess a large carrier mobility (>10^3 cm^2 V^{-1} s^{-1}) and substantial elasticity at room temperature.[51,52] Moreover, InSe holds the promise of becoming a critical component in opto-/photoelectronic devices[53] and catalysts,[54] owing to its band gap in the visible regime, active electronic edge states, and ambient stability.[53−56] Additionally, InSe 2D flakes are readily synthesized via liquid-phase exfoliation,[54] foregoing the need for substrate growth or precursor synthesis (common drawbacks of alternative methods such as chemical vapor deposition), while minimizing processing time. Altogether, these facts continue to support 2D InSe as a particularly promising strain-tunable thermoelectric material awaiting further exploration.

In the present work, we study the thermoelectric properties of uniaxially strained β-InSe using the generalized gradient approximation (GGA)[57] within density functional theory (DFT) in Quantum ESPRESSO (QE)[58,59] and by solving the Boltzmann Transport Equation (BTE) with BoltzTrap[60] and ShengBTE.[61] Our uniaxial compression study explores a unique set of anisotropic properties previously unexplored in the literature,[62] revealing stark directional discrepancies in monolayer β-InSe's transport phenomena that may be useful in future thermoelectric applications. Throughout this work, we apply this uniaxial strain along the zigzag direction. We demonstrate that a band convergence within the conduction bands occurs at a uniaxial compressive strain of −6%, around which a significant enhancement of ZT is observed in p-type InSe at room temperature. As uniaxial strain is further applied, valence bands also begin to merge and thus further increase ZT to a maximum of 0.46. We furthermore investigate the temperature and carrier concentration dependencies of InSe's transport coefficients in the presence of strain and discuss their relationship with the band convergence we observe. Our results demonstrate the utility of strain engineering for designing the highly efficient thermoelectric materials of the future.

METHODS

We carried out first-principles calculations using the GGA in DFT with the Quantum ESPRESSO program.[58,59,63,64] The calculations were performed using the Perdew−Burke−Ernzerhof (PBE)[57] exchange-correlation functional with GBRV Ultra-Soft Pseudopotentials (USPP).[65] The Brillouin zone integrations were carried out using a 10 × 10 × 1 k-point mesh with a plane-wave kinetic energy cutoff of 45 Ry and a charge density cutoff energy of 540 Ry in the self-consistent calculation. A 40 × 40 × 1 k-point grid was used for calculating the electronic density of states (DOS) in the non-self-consistent calculation. We have used the Methfessel−Paxton (MP) smearing method[66] with a smearing width of 0.01 Ry to compute band structures and densities of states. Computa-

DOI: 10.1021/acs.jpcc.9b05681
J. Phys. Chem. C 2019, 123, 25437−25447

tional results for the electronic properties of β-InSe were obtained without spin polarization or spin orbit coupling.

In order to remove spurious interactions between layers, we used a vacuum spacing of 30 Å along the c axis. The 2D InSe primitive unit used, shown in Figure 1, exhibits a hexagonal

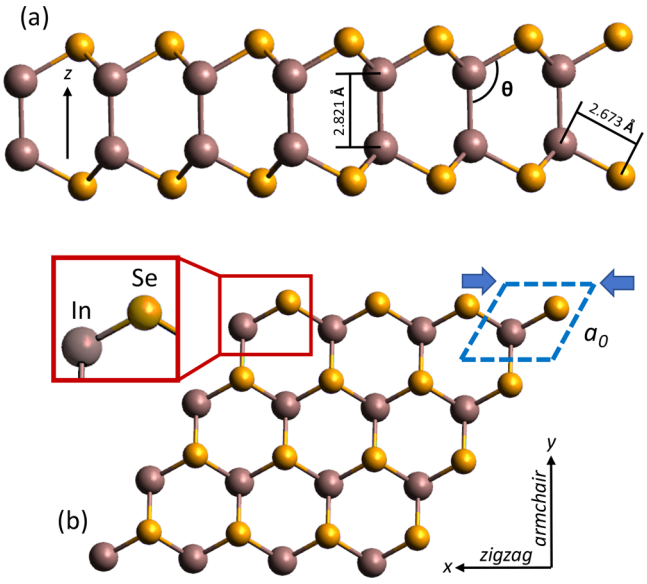

Figure 1. Crystal structure of monolayer β-InSe: (a) side view, illustrating the monolayer configuration; (b) top view, elucidating the hexagonal unit cell character. As indicated in the red (solid line) inset of (b), indium is denoted in purple-gray and selenium in orange. The unit cell geometry, lattice parameter (a_0), and the direction along which the compressive strain was applied are depicted using the dashed blue diamond. Average bond distances and angles are denoted in angstroms and degrees, respectively, with θ = 118.9°.

crystal structure. Formation of the monolayer is generated by repeating the Se−In−In−Se unit in the xy plane, resulting in the recognizable honeycomb lattice (Figure 1a,b).

Thermoelectric transport coefficients such as the Seebeck coefficient, electrical conductivity, and electronic contribution to the thermal conductivity were obtained with BoltzTrap's smooth Fourier expansion method of solving the BTE under the relaxation time approximation (RTA) in terms of carrier concentration.[60] We estimate the strain dependence of the effective mass, m^*, and the relaxation time, τ, for both hole and electron carriers.

Using BoltzTrap, the properties S, σ/τ, and κ_e/τ were each computed as a function of carrier concentration and temperature for each compressive strain. In order to extract transport coefficients from BoltzTrap for complete ZT calculations, we must separately calculate the relaxation time, $\tau = (m^*)\mu/e$, where m^* is the effective mass:

$$m^* = \hbar^2\left(\frac{\partial^2 E(k)}{\partial k^2}\right)^{-1} \tag{3}$$

and μ is the electron mobility, determined from deformation potential theory (DPT) based on the effective mass approximation:[35,67−69]

$$\mu = \frac{2e\hbar^3 C^{2D}}{3k_B T|m^*|^2 E_1^2} \tag{4}$$

In the above, $C^{2D} = (\partial^2 E_T/\partial\delta^2)/S_0$ is the elastic modulus for layered two-dimensional systems and $E_1 = \partial\varepsilon_b/\partial\delta$ is the deformation constant, with δ describing the applied strain, S_0 is the area of the system, and E_T (ε_b) is the total (band-edge) energy.

To obtain the lattice thermal conductivity, the calculation of both second-order (i.e., harmonic) and third-order (i.e., anharmonic) interatomic force constants (IFC) is required. All calculations associated with the coupling between atoms were performed within DFT and density-functional perturbation theory (DFPT) using the QE package. A 12 ×12 × 1 q-point grid (6 × 6 × 1 supercells of Γ-point only) was used for calculating the harmonic (anharmonic) IFCs. Interactions between fifth-nearest neighbors corresponding to 220 different configurations for the hexagonal supercell in our work were taken into account for the anharmonic IFCs. Phonon BTE calculations were conducted using ShengBTE,[61,70] including the Python code *thirdorder.py* for convenient reconstruction of the entire IFC matrix for use in QE,[71] and used to predict material properties as well as the lattice thermal conductivity using *ab initio* results as inputs.

RESULTS AND DISCUSSION

Electronic Structure Calculations. As a first step toward determining the thermoelectric properties of β-InSe, we employed DFT using the Perdew−Burke−Ernzerhof (PBE)[57] functional to obtain β-InSe's geometry and band structure under compressive strains ranging from 0 to −7%. (All of the work reported herein refers to the β phase of InSe.) β-InSe was chosen because of its anticipated stability.[55] All compressive strains were exerted along the zigzag direction, as depicted in Figure 1. In the absence of strain, we obtained a lattice constant of 3.998 Å, an In−Se (In−In) bond length of 2.673 Å (2.821 Å), and an Se−In−In bond angle of 118.9° (see Figure 1). Table 1 presents our computed band gaps, all indirect with a 1.51 eV gap at 0% strain. All of these values are in strong agreement with those presented in previous DFT/PBE studies.[46,72]

Table 1. Band Gap, E_g, Effective Mass (m_e^* (m_h^*)), and Relaxation Time (τ_e (τ_h)) for Electrons (Holes) in the Presence of Strain, δ, up to −7% at T = 300 K[a]

δ (%)	m_e^*/m_0	τ_e (10^{-14} s)	m_h^*/m_0	τ_h (10^{-14} s)	E_g (eV)
0	0.185	9.274	2.065	86.36	1.51
−1	0.184	9.343	2.100	84.90	1.56
−2	0.185	9.302	2.140	83.33	1.62
−3	0.187	9.214	1.939	91.97	1.67
−4	0.191	9.024	1.868	95.45	1.72
−5	0.190	9.071	1.764	101.11	1.77
−6	0.192	8.958	1.632	109.23	1.82
−7	0.194	8.844	1.478	120.67	1.86

[a]Here, m_0 is the electron rest mass. All calculations were performed at the PBE level.

As also clear from Table 1, band gaps grow with increased compressive strain. This is as expected when compared with other 2D materials; phosphorene's band gap, for instance, also increases with increased strain.[35] InSe's band gap ranges from 1.51 to 1.86 eV over the −7% compression, reminiscent of the change in the band gap from the 1.4 eV observed in bulk InSe to the 2.6 eV observed in monolayer InSe,[73] which further exemplifies InSe's tunability.

DOI: 10.1021/acs.jpcc.9b05681
J. Phys. Chem. C 2019, 123, 25437−25447

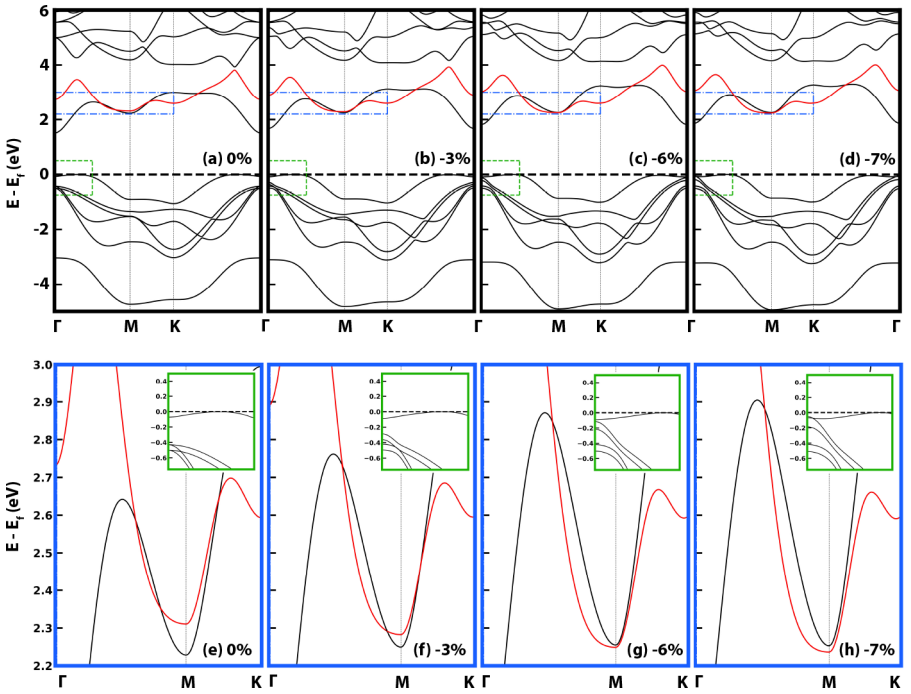

Figure 2. Band structure of an InSe monolayer under compressive strain. Top: entire *k*-path band structure as a function of compressive strain. Bottom: expanded Γ−M−K region of the conduction band (blue box), illustrating band convergence. Second lowest conduction band highlighted in red. Inset (green box) illustrates valence band convergence around Γ point.

It is important to note our reason for selecting a GGA-PBE functional rather than various forms of hybrid functionals. For transport phenomena, band curvature is vital as it captures properties such as reduced mass to calculate electron mobility. Band gap values are less pivotal, as we sample across the gap to include both valence and conductance bands regardless, in order to capture the curvature for transport properties. GGA-PBE is known to underestimate the band gap of similar materials, unlike certain hybrid functionals (e.g., HSE06); however, the band curvature between functionals has not been observed to substantially change. DFT studies of InSe, in particular, are able to use a simple scissoring correction to adjust the band gap of GGA-PBE to coincide with hybrid functional band gap results, essentially matching the band diagrams generated by the hybrid functional alone because the curvature remains consistent.[73] In essence, despite GGA-PBE's underestimation of the band gap, we are able to reliably calculate transport properties at a more reasonable computational cost because of the sufficiently accurate curvature GGA yields.

More interesting than how the band gaps change is how the full band structures presented in Figure 2 vary with compressive strain. Close inspection of the conduction bands in the region between the Γ and M points reveals a band convergence at the M point. As the compressive strain is increased to −6%, the second lowest conduction band (LCB) becomes equivalent in energy to the 0% compression LCB at the M point. Upon surpassing −6% compression, the higher energy band across the rest of the *k*-point path replaces the original LCB at the M point. Despite these changes, excitation still occurs indirectly from a point between the valence Γ and M points to the conduction Γ point, but the LCB state has switched at the M point. Altogether, the switching of the conduction band minimum state with a higher energy state through strain resulted in band convergence and an overall increase of the band gap.

The valence bands undergo notable shifts in energy in response to increased compressive strain as well. Also at −6% strain, but at the Γ point, we observe the second and third highest valence bands increase in energy, closing the energy gap between the highest energy valence band (see inset of Figure 2). A flattening of these three bands from the Γ point toward the M point (and K point) drastically increases the number of available states near the Fermi level, which likely improves the p-type conductivity of monolayer InSe under strains greater than −6% due to the dominance of hole carriers in the valence bands.

Relaxation Time. In this work, we consider the relaxation time for both holes and electrons. Although caution was taken in calculating τ by using dense *k*-point sampling and curvature fitting, it is important to note that errors in our estimates may arise from inaccuracies within DFT calculations of the band structures, as well as inaccuracies in the way in which those bands were fit to estimate reduced masses.

Our calculations estimate the elastic modulus, C^{2D}, for InSe to be 85.46 N/m, which is somewhat smaller than values previously reported for phosphorene (∼106 N/m),[35] MoS_2 (∼120 N/m),[74] and graphene (∼342 N/m),[75] but within expectations. The InSe deformation constant, E_1, is found to be 6.334 eV for electrons and 0.622 eV for holes. The previously estimated value of E_1 in monolayer phosphorene is 3.98 eV for electrons,[35] thus also placing our estimates within the expected range for 2D material deformation constants.

Table 1 summarizes the relaxation times and effective masses in InSe for both holes and electrons in the presence of strains up to −7% at room temperature (T = 300 K). As can be seen in Table 1, both the effective masses and relaxation times for p-type (hole carrier) InSe are almost 1 order of magnitude larger than those for n-type (electron carrier) InSe. This

DOI: 10.1021/acs.jpcc.9b05681
J. Phys. Chem. C 2019, 123, 25437−25447

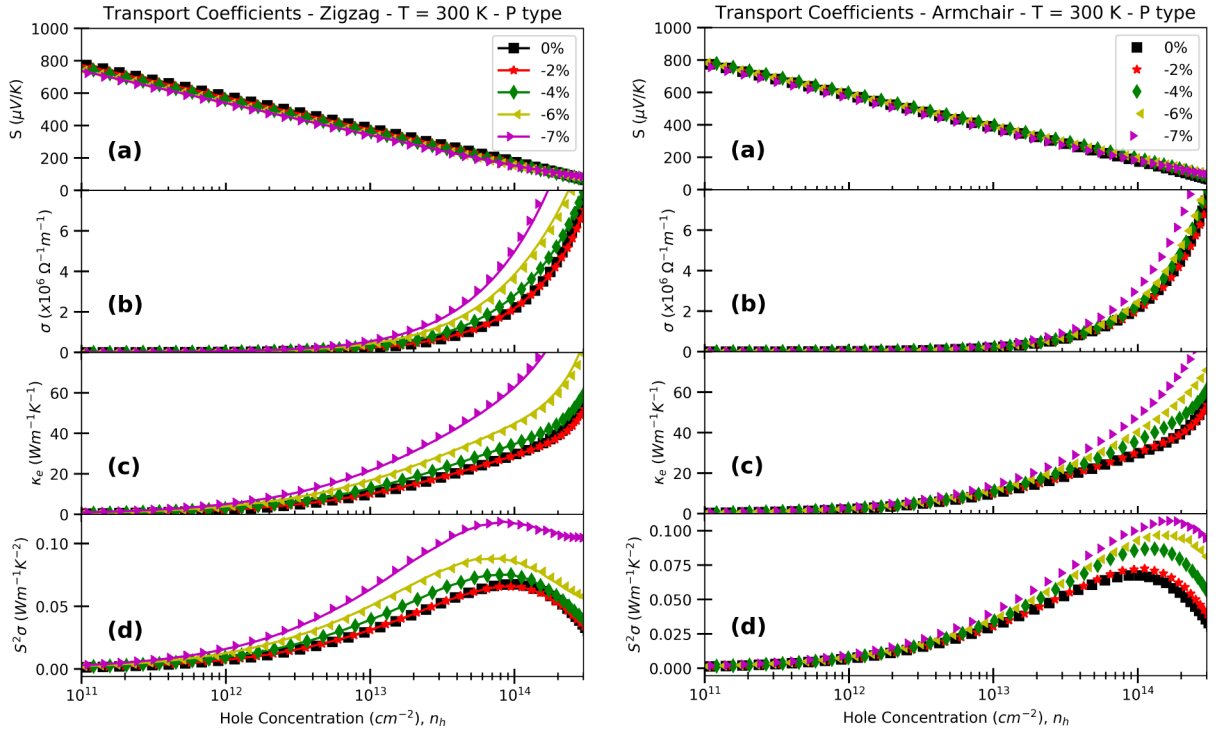

Figure 3. Thermoelectric transport properties of p-type InSe along the zigzag (left) and armchair (right) directions as a function of hole concentration in the presence of uniaxial strains at T = 300 K. From top to bottom: (a) Seebeck coefficient, (b) electrical conductivity, (c) electronic thermal conductivity, and (d) power factor.

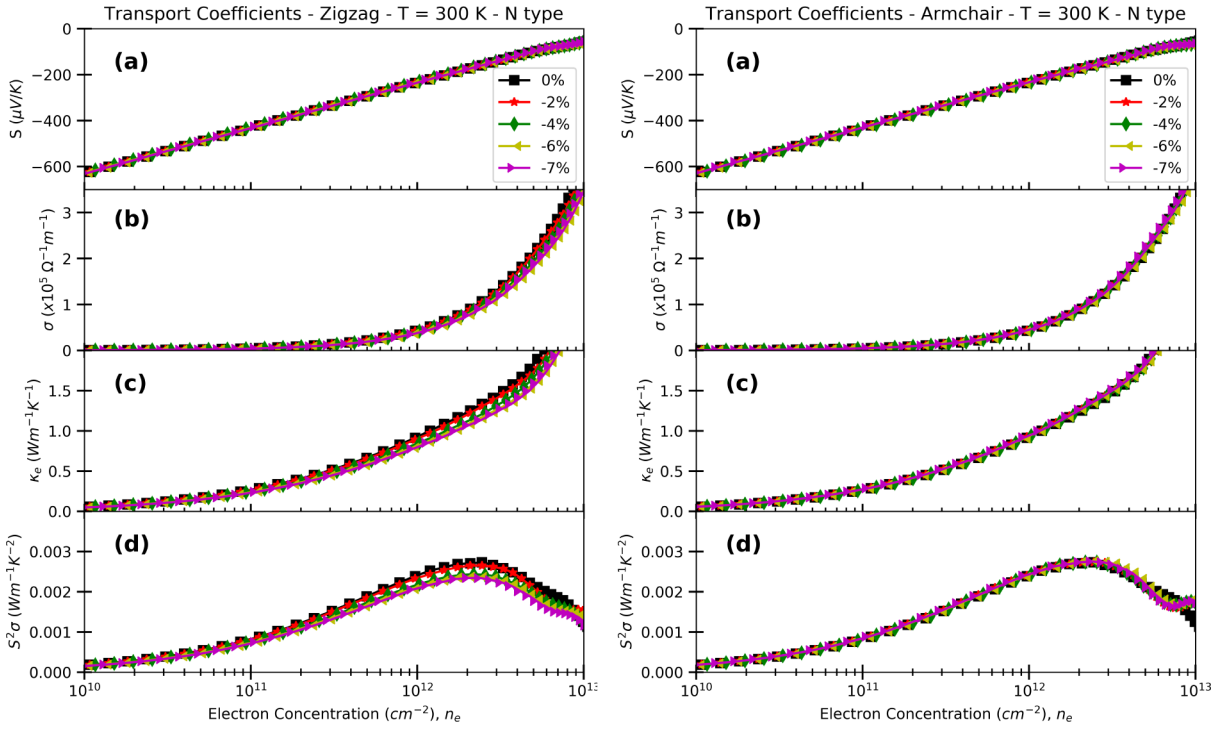

Figure 4. Thermoelectric transport properties of n-type InSe along the zigzag (left) and armchair (right) directions as a function of electron concentration in the presence of uniaxial strains at T = 300 K. From top to bottom: (a) Seebeck coefficient, (b) electrical conductivity, (c) electronic thermal conductivity, and (d) power factor.

suggests that p-type InSe is preferential for thermoelectric applications, because larger effective masses usually correlate with enhanced electrical conduction, likely leading to larger values of ZT.

Transport Coefficients. Analysis of InSe's transport coefficients further reveals the complex nature of optimizing ZT, as given by eq 1, for real-world applications. In order to ensure that our simulations correspond to realizable materials, we restrict our carrier concentrations (both electron and hole)

DOI: 10.1021/acs.jpcc.9b05681
J. Phys. Chem. C 2019, 123, 25437−25447

to lie in a range between 10^{11} and 10^{15} cm^{-2}, as observed in other 2D materials. Figures 3 and 4 summarize the thermoelectric transport properties of p- and n-type InSe in both the zigzag and armchair directions as functions of the hole and electron concentrations, in the presence of uniaxial strain at room temperature (300 K). For more details, please see the Supporting Information.

As can be seen in Figures 3a and 4a for both the zigzag and armchair directions, the Seebeck coefficient is positive for p-type InSe and negative for n-type InSe, both assuming a power law dependence on carrier density. Even though the Seebeck coefficient's magnitude decreases as a function of both the hole and electron carrier densities (Figures 3a and 4a), the electrical conductivity (Figures 3b and 4b), and electronic thermal conductivity (Figures 3c and 4c) increase over the entire carrier density range: $10^{11} < n_h < 3 \times 10^{14}$ for holes and $10^{10} < n_e < 10^{13}$ for electrons.

As depicted in both panels of Figure 3a, p-type InSe's Seebeck coefficient changes minimally with strain both in the zigzag and armchair directions. The Seebeck coefficient along the zigzag direction undergoes a maximum 36 μV/K decline over the range of compression studied (a 4.7% reduction overall), while the Seebeck coefficient along the armchair direction undergoes less than a 20 μV/K decline over the same range (about 2% reduction). N-type InSe's Seebeck coefficient changes even less, exhibiting a maximum decrease of 5 μV/K (<1%). These results demonstrate that the Seebeck coefficient has a small to negligible effect on the changes to ZT that we observe upon compressing InSe.

As expected, the electrical conductivity σ of hole carriers in both panels of Figure 3b is almost 1 order of magnitude larger than that of the electron carriers in both panels of Figure 4b. This is because the largest effective masses, which lead to the largest conductivities, were associated with the highest valence band whose electrical properties are dominated by holes (see Table 1). Most of the significant differences in transport properties occur between a hole carrier concentration of 10^{13} and 10^{14} in p-type InSe and an electron carrier concentration around 10^{12} in n-type InSe.

Both σ and κ_e increase much more significantly than the Seebeck coefficient for p-type InSe. σ in the zigzag direction increases from 1×10^6 to 3×10^6 Ω^{-1} m^{-1} (a 25−100% gain), while σ in the armchair direction increases by a factor of 1×10^6 Ω^{-1} m^{-1} at a hole concentration of 10^{14} cm^{-2} (a 25% gain) with increasing compressive strain. Increases in σ more than compensate for decreases in the Seebeck coefficient across the hole concentration range. κ_e in the zigzag and armchair directions for p-type InSe increases by about 20 W m^{-1} K^{-1} (a 50% gain). κ_e's relative increase is similar to σ's relative increase, but its overall change in magnitude is much smaller and thus ultimately only negligibly impacts ZT.

Both electrical conductivity (both panels in Figure 3b) and electronic thermal conductivity (both panels in Figure 3c) in p-type InSe continue to increase under strains up to −7%, revealing minimal dependence upon band phenomena. The σ of p-type InSe continues to increase, compensating for the simultaneous increase of its κ_e, beyond the band convergent strain of −6%, while the σ and κ_e of n-type InSe decrease (albeit at a much smaller rate) until −6% compression. The electrical conductivity of p-type InSe continues to increase beyond −6% compression because of the emergence of additional band degeneracies in the valence band, which is dominated by hole carriers, around −7% (see Figure 2).

In contrast, the electrical conductivity of n-type InSe decreases as a function of strain, and remains roughly constant beyond −6%, at which point the previously degenerate conduction bands cross. N-type InSe's σ and κ_e change by less than 1% under uniaxial compression, and thus have a negligible impact on ZT. It should nevertheless be observed that uniaxial strain impacts σ and κ_e in opposite ways: As compressive strain increases, n-type σ and κ_e values decrease, whereas p-type σ and κ_e values increase. The inverse nature of these changes with respect to doping type will result in opposing effects on ZT.

Prior to calculating ZT, the numerator (which excludes both the electronic and lattice thermal conductivities) is calculated as a preliminary assessment of material promise; this quantity is commonly referred to as the power factor (PF). In Figures 3 and 4, plot (d) shows PF results for p- and n-type InSe. The PF for p-type (n-type) InSe has a peak at around $n_h \sim 10^{14}$ ($n_e \sim 10^{12}$), which are carrier concentrations that have previously been shown to be attainable within 2D thermoelectric materials.

Our results show that the effect of strain on p-type InSe is remarkable, resulting in a nearly 2-fold magnification of the power factor, even though no significant changes were observed in n-type InSe. The optimal PF is obtained at the maximal strain in the zigzag direction (−7%) and nearer the band convergent strain in the armchair direction (around −6%). In order to assess the full impact of these individual properties on both p- or n-type InSe's ZT value, however, we must also consider the lattice thermal conductivity.

In Figure 5, we present the lattice thermal conductivity of InSe, κ_{ph}, without strain as a function of temperature, T. κ_{ph}

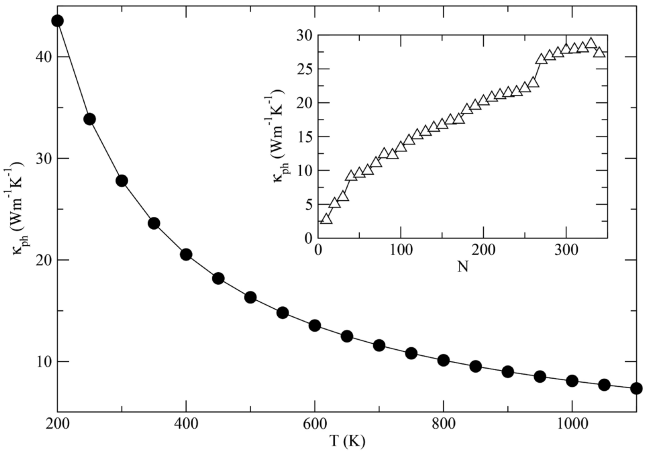

Figure 5. Lattice thermal conductivity, κ_{ph}, of InSe as a function of temperature, T, on a $300 \times 300 \times 1$ q-point grid. The inset shows κ_{ph} at T = 300 K as a function of N with $N \times N \times 1$ q-point grids.

decreases with increasing T and shows $1/T$ dependence at high temperatures. As shown in the inset of Figure 5, κ_{ph} converges for $N > 270$, where N represents the q-point grid size, which supports our use of a large q-point grid. We find that the calculated κ_{ph} is 27.79 W m^{-1} K^{-1} at T = 300 K using a q-point grid of $300 \times 300 \times 1$, which is within range of previous estimates.[46,76] However, other studies have shown that κ_{ph} depends on sample size. In general, as sample size decreases, κ_{ph} decreases because there is less material through which heat can disperse, and in the bulk, there tend to be more grain boundaries which further inhibit a material's ability to

DOI: 10.1021/acs.jpcc.9b05681
J. Phys. Chem. C 2019, 123, 25437−25447

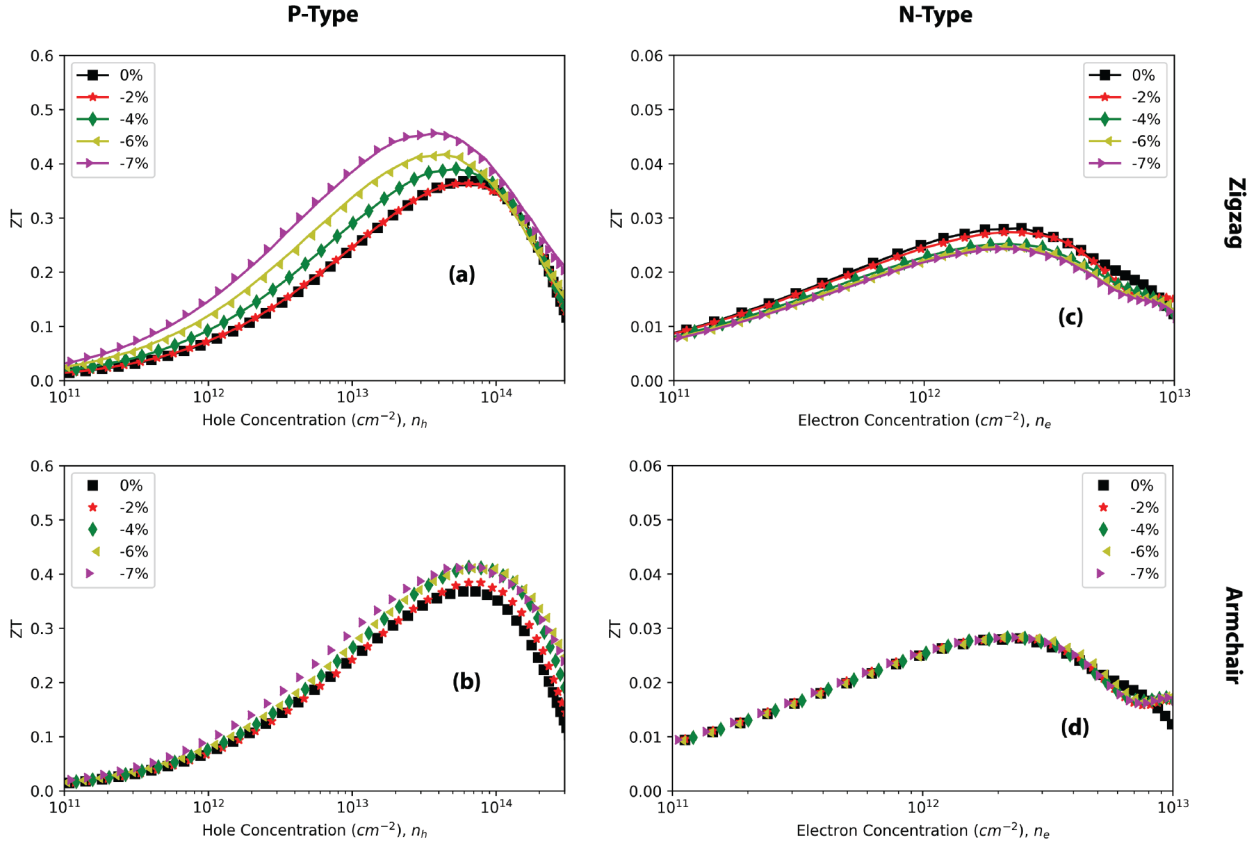

Figure 6. Dimensionless figure of merits, ZT, as a function of carrier concentrations in the presence of uniaxial strains at T = 300 K for p-type (left) and n-type (right) InSe along the zigzag (top) and armchair (bottom) directions.

distribute thermal energy. In fact, nanoscale samples have been predicted to reduce κ_{ph} by more than half,[46] implying that our κ_{ph} estimates may be viewed as upper bounds to the true κ_{ph} values; therefore, our ZT estimates are lower bounds for monolayer InSe.

Figure of Merit, ZT. In Figure 6, we summarize the strain dependence of ZT with respect to hole and electron carrier densities in both the zigzag and armchair directions. We obtain a maximum p-type ZT value of 0.46 at −7% strain at 300 K for hole carriers along the zigzag direction, and a maximum of 0.41 at −5% strain for hole carriers along the armchair direction (Figure 6a,b, respectively). While the p-type power factor increases by a factor of 2 with strain, after changes in κ_{ph} were taken into consideration, the p-type ZT ultimately changes by a factor of 1/3 (a 30% increase from relaxed InSe). The n-type ZT values only reach 0.026 in the zigzag direction and 0.029 along the armchair direction and were thus an order of magnitude smaller than the p-type ZT values. Figure S6 more explicitly illustrates this dramatic difference between carrier type ZT values. Overall, these results demonstrate that p-type InSe exhibits superior performance compared to its n-type counterpart and is more susceptible to tuning via compressive strain engineering.

These ZT zigzag and armchair direction maxima coincide with the valence and conduction band convergence phenomena described earlier. The p-type InSe's maximum ZT occurs at −7% strain, in the vicinity of the conduction band convergence at the M point we observe at −6% strain and the valence band degeneracy that emerges at the Γ point between −6 and −7% strain (see Figure 2). Because ZT achieves its maximum at the strains at which band convergence occurs, our ZT results reinforce the idea that materials that exhibit band convergence may be most useful for thermoelectric engineering.[77−79]

In Tables 2 and 3, we summarize the carrier concentrations that maximized ZT in different directions for varying strains.

Table 2. Hole Concentrations (n_h) in Both the Zigzag (zz) and Armchair (ac) Directions That Maximize the InSe ZT in the Presence of up to −7% Strain, δ, at T = 300 K[a]

δ (%)	n_h^{zz} (10^{13} cm^{-2})	$ZT_{h,zz}^{max}$	n_h^{ac} (10^{13} cm^{-2})	$ZT_{h,ac}^{max}$
0	**5.923**	**0.3679**	**5.923**	**0.3679**
−1	6.209	0.3666	6.209	0.3801
−2	6.452	0.3637	7.845	0.3839
−3	5.719	0.3850	7.001	0.4075
−4	5.275	0.3905	6.478	0.4126
−5	4.204	0.4005	**7.721**	**0.4134**
−6	4.312	0.4169	6.468	0.4107
−7	**3.909**	**0.4563**	7.067	0.4128

[a]Minima and maxima are given in bold.

The carrier concentration that maximizes ZT steadily declines for all strains, echoing the Seebeck coefficient's reduction overall and a reduced ability to utilize larger concentrations of hole carriers.

The ZT values for p-type InSe predicted by our first-principles calculations were within range of those predicted analytically for low-dimensional InSe,[80] but only when InSe is strained. Without strain, ZT reaches a maximum of 0.37 along the zigzag direction; with strain, this value increases to 0.46. To place these room-temperature ZT values in context, copper

DOI: 10.1021/acs.jpcc.9b05681
J. Phys. Chem. C 2019, 123, 25437−25447

Table 3. Electron Concentrations (n_e) in Both the Zigzag (zz) and Armchair (ac) Direction That Maximize the InSe ZT in the Presence of up to −7% Strain, δ, at T = 300 K[a]

δ (%)	n_e^{zz} (10^{13} cm^{-2})	$ZT_{e,zz}^{max}$	n_e^{ac} (10^{13} cm^{-2})	$ZT_{e,ac}^{max}$
0	**3.165**	**0.01099**	**3.165**	**0.01099**
−1	2.947	0.01850	2.947	0.01886
−2	2.411	0.02196	2.411	0.02272
−3	**2.145**	**0.02621**	2.145	0.02844
−4	1.718	0.02522	1.718	0.02826
−5	1.236	0.02542	**1.236**	**0.02891**
−6	1.038	0.02465	1.038	0.02843
−7	1.048	0.02433	1.048	0.02832

[a]Minima and maxima are given in bold.

sulfide alloys fluctuate around a ZT of 0.2, and even promising bismuth alloys such as BiCuSeO vary around a ZT of only 0.5.[81,82] Our predicted ZT values, both strained and unstrained, are therefore reasonable to anticipate in future experiments on monolayer β-InSe.

CONCLUSION

In conclusion, we have studied the directional thermoelectric properties of monolayer InSe under strain as a function of both hole and electron carrier densities using first-principles simulations conjoined with BTE calculations. Our numerical results suggest that p-type InSe is superior to n-type InSe, manifesting ZT values an order of magnitude larger over a wide range of compressive uniaxial strains. Our calculations demonstrate a band convergence at the M point under a strain of −6%, at which point a significant magnification occurs; transport coefficients lead to a 2-fold increase in the PF and a 30% increase overall in the room temperature ZT for p-type InSe. Beyond the band convergent strain of −6%, valence bands also begin to merge, causing the p-type σ to continue to grow and resulting in further ZT increases. The importance of strain is directly reflected by the enhanced power factor and p-type σ in all directions around the band degenerate strain. Our studies demonstrate that strain engineering is a viable pathway to engineering band structure and transport coefficients, which is vital for realizing improved thermoelectric materials.

Other materials in this family of indium chalcogenide monolayers, such as InS or InTe, were also examined during our selection of which alloy to explore for thermoelectric merit; however, we did not observe a band convergence for InS as we did with InSe, which would have also promised some enhancement of transport properties. In our preliminary studies, InTe was observed to manifest the indicative band convergences; however, InSe is more experimentally accessible[83,84] and therefore more relevant. Significant research has already gone into the thermoelectric properties of the gallium chalcogenides.[85,86]

Given the approximations inherent within any computational treatments of materials, experimental efforts aimed at establishing the ranges of realizable carrier concentrations, strains, thermal conductivities, and ZTs would be welcome. We particularly invite experimental measurements of κ_{ph} for monolayer InSe, as such measurements would resolve literature discrepancies. One further possible step would be measurement of InSe's κ_{ph} under strain, which would be beneficial for demonstrating whether uniaxially broken symmetry also results in reduced κ_{ph} values, as was observed in recent work by Vega-Flick et al.,[87] or in enhanced κ_{ph} values as observed by Meng et al.[88]

In order to perform these measurements, researchers will have to synthesize monolayer InSe flakes in sufficient abundance. This remains a challenge, especially for strain studies, as many flakes decompose within several days when exposed to air at ambient conditions; few-layer InSe is significantly more stable.[89] Recently, liquid-phase exfoliation techniques have improved the abundance and expedience of synthesizing InSe monolayers,[54] promising sufficient quantity for strain testing in the future. An additional challenge will be developing the appropriate methodology and equipment to apply uniaxial strain to an InSe monolayer. Cantilever,[90] substrate,[91] and suspension[92] techniques have been applied to graphene, and hydrostatic pressurization[88] has been applied to MoS_2 to achieve the strains described here. These techniques await adaptation to InSe monolayers.

ASSOCIATED CONTENT

Supporting Information

The Supporting Information is available free of charge on the ACS Publications website at DOI: 10.1021/acs.jpcc.9b05681.

Further discussion of zigzag and armchair directionality in 2D materials and the possible z-directional contributions to transport phenomena in 2D InSe (PDF)

AUTHOR INFORMATION

Corresponding Author

*E-mail: jeongpilsong@gmail.com.

ORCID

Leonard W. Sprague, Jr.: 0000-0003-1926-8827

Notes

The authors declare no competing financial interest.

ACKNOWLEDGMENTS

This work was supported by U.S. National Science Foundation Grant No. DMR-1726213. Calculations were performed using resources at the Center for Computation and Visualization, Brown University, which is supported by NSF Grant No. ACI-1548562.

REFERENCES

(1) He, J.; Tritt, T. M. Advances in thermoelectric materials research: Looking back and moving forward. *Science* **2017**, *357*, No. eaak9997.

(2) Tritt, T. M.; Böttner, H.; Chen, L. Thermoelectrics: Direct Solar Thermal Energy Conversion. *MRS Bull.* **2008**, *33*, 366−368.

(3) Tritt, T. M.; Subramanian, M. A. Thermoelectric Materials, Phenomena, and Applications: A Bird's Eye View. *MRS Bull.* **2006**, *31*, 188−198.

(4) Snyder, G. J.; Toberer, E. S. Complex thermoelectric materials. *Nat. Mater.* **2008**, *7*, 105−114.

(5) *Estimated U.S. Energy Consumption in 2017: 97.7 Quads*; LLNL, U.S. Department of Energy, 2018.

(6) Ioffe, A. *Semiconductor Thermoelements and Thermoelectric Cooling*; InfoSearch: London, 1957.

(7) Nolas, G. S.; Sharp, J.; Goldsmid, J. *Thermoelectrics: Basic Principles and New Materials Developments*; Springer Series in Materials Science; Springer-Verlag: Berlin Heidelberg, 2001.

(8) Kanatzidis, M. G., Hogan, T. P., Mahanti, S. D., Eds. *Chemistry, Physics, and Materials Science of Thermoelectric Materials: Beyond Bismuth Telluride*; Fundamental Materials Research; Springer US, 2003.

DOI: 10.1021/acs.jpcc.9b05681
J. Phys. Chem. C 2019, 123, 25437−25447

(9) Goldsmid, H. J. In *Introduction to Thermoelectricity*; Springer Series in Materials Science; Springer: Berlin, Heidelberg, 2016; pp 1−7.
(10) Wickramaratne, D.; Weston, L.; Van de Walle, C. G. Monolayer to Bulk Properties of Hexagonal Boron Nitride. *J. Phys. Chem. C* **2018**, *122*, 25524−25529.
(11) Saeed, Y.; Kachmar, A.; Carignano, M. A. First-Principles Study of the Transport Properties in Bulk and Monolayer MX3 (M = Ti, Zr, Hf and X = S, Se) Compounds. *J. Phys. Chem. C* **2017**, *121*, 1399−1403.
(12) Poudel, B.; Hao, Q.; Ma, Y.; Lan, Y.; Minnich, A.; Yu, B.; Yan, X.; Wang, D.; Muto, A.; Vashaee, D.; et al. High-Thermoelectric Performance of Nanostructured Bismuth Antimony Telluride Bulk Alloys. *Science* **2008**, *320*, 634−638.
(13) Venkatasubramanian, R.; Siivola, E.; Colpitts, T.; O'Quinn, B. Thin-film thermoelectric devices with high room-temperature figures of merit. *Nature* **2001**, *413*, 597−602.
(14) Goldsmid, H. J.; Giutronich, J. E.; Kaila, M. M. Solar thermoelectric generation using bismuth telluride alloys. *Sol. Energy* **1980**, *24*, 435−440.
(15) Mishra, S. K.; Satpathy, S.; Jepsen, O. Electronic structure and thermoelectric properties of bismuth telluride and bismuth selenide. *J. Phys.: Condens. Matter* **1997**, *9*, 461.
(16) Li, F.; Zhai, R.; Wu, Y.; Xu, Z.; Zhao, X.; Zhu, T. Enhanced thermoelectric performance of n-type bismuth-telluride-based alloys via In alloying and hot deformation for mid-temperature power generation. *Journal of Materiomics* **2018**, *4*, 208−214.
(17) Hong, M.; Chen, Z.-G.; Zou, J. Fundamental and Progress of Bi2Te3-based Thermoelectric Materials. *Chin. Phys. B* **2018**, *27*, No. 048403.
(18) Wright, D. A. Thermoelectric Properties of Bismuth Telluride and its Alloys. *Nature* **1958**, *181*, 834.
(19) Heremans, J. P.; Jovovic, V.; Toberer, E. S.; Saramat, A.; Kurosaki, K.; Charoenphakdee, A.; Yamanaka, S.; Snyder, G. J. Enhancement of Thermoelectric Efficiency in PbTe by Distortion of the Electronic Density of States. *Science* **2008**, *321*, 554−557.
(20) Fu, T.; Yue, X.; Wu, H.; Fu, C.; Zhu, T.; Liu, X.; Hu, L.; Ying, P.; He, J.; Zhao, X. Enhanced thermoelectric performance of PbTe bulk materials with figure of merit zT > 2 by multi-functional alloying. *Journal of Materiomics* **2016**, *2*, 141−149.
(21) Harman, T. C.; Taylor, P. J.; Walsh, M. P.; LaForge, B. E. Quantum Dot Superlattice Thermoelectric Materials and Devices. *Science* **2002**, *297*, 2229−2232.
(22) Zhao, L.-D.; Lo, S.-H.; Zhang, Y.; Sun, H.; Tan, G.; Uher, C.; Wolverton, C.; Dravid, V. P.; Kanatzidis, M. G. Ultralow thermal conductivity and high thermoelectric figure of merit in SnSe crystals. *Nature* **2014**, *508*, 373−377.
(23) Duong, A. T.; Nguyen, V. Q.; Duvjir, G.; Duong, V. T.; Kwon, S.; Song, J. Y.; Lee, J. K.; Lee, J. E.; Park, S.; Min, T. Achieving ZT = 2.2 with Bi-doped n-type SnSe single crystals. *Nat. Commun.* **2016**, *7*, 13713.
(24) Heremans, J. P.; Dresselhaus, M. S.; Bell, L. E.; Morelli, D. T. When thermoelectrics reached the nanoscale. *Nat. Nanotechnol.* **2013**, *8*, 471−473.
(25) Heremans, J.; Thermoelectricity, P. The ugly duckling. *Nature* **2014**, *508*, 327−328.
(26) Hicks, L. D.; Dresselhaus, M. S. Thermoelectric figure of merit of a one-dimensional conductor. *Phys. Rev. B: Condens. Matter Mater. Phys.* **1993**, *47*, 16631−16634.
(27) Hicks, L. D.; Dresselhaus, M. S. Effect of quantum-well structures on the thermoelectric figure of merit. *Phys. Rev. B: Condens. Matter Mater. Phys.* **1993**, *47*, 12727−12731.
(28) Chen, K.-X.; Li, M.-S.; Mo, D.-C.; Lyu, S.-S. Nanostructural thermoelectric materials and their performance. *Front. Energy* **2018**, *12*, 97−108.
(29) Nika, D. L.; Ghosh, S.; Pokatilov, E. P.; Balandin, A. A. Lattice thermal conductivity of graphene flakes: Comparison with bulk graphite. *Appl. Phys. Lett.* **2009**, *94*, 203103.
(30) Gandi, A. N.; Schwingenschlögl, U. Thermal conductivity of bulk and monolayer MoS 2. *EPL* **2016**, *113*, 36002.
(31) Sahoo, S.; Gaur, A. P. S.; Ahmadi, M.; Guinel, M. J.-F.; Katiyar, R. S. Temperature-Dependent Raman Studies and Thermal Conductivity of Few-Layer MoS2. *J. Phys. Chem. C* **2013**, *117*, 9042−9047.
(32) Anno, Y.; Imakita, Y.; Takei, K.; Akita, S.; Arie, T. Enhancement of graphene thermoelectric performance through defect engineering. *2D Mater.* **2017**, *4*, No. 025019.
(33) Tran, V.-T.; Saint-Martin, J.; Dollfus, P.; Volz, S. Optimizing the thermoelectric performance of graphene nano-ribbons without degrading the electronic properties. *Sci. Rep.* **2017**, *7*, 2313.
(34) Butler, S. Z.; Hollen, S. M.; Cao, L.; Cui, Y.; Gupta, J. A.; Gutiérrez, H. R.; Heinz, T. F.; Hong, S. S.; Huang, J.; Ismach, A. F.; et al. Progress, Challenges, and Opportunities in Two-Dimensional Materials Beyond Graphene. *ACS Nano* **2013**, *7*, 2898−2926.
(35) Lv, H. Y.; Lu, W. J.; Shao, D. F.; Sun, Y. P. Enhanced thermoelectric performance of phosphorene by strain-induced band convergence. *Phys. Rev. B: Condens. Matter Mater. Phys.* **2014**, *90*, 085433.
(36) Peng, X.; Wei, Q.; Copple, A. Strain-engineered direct-indirect band gap transition and its mechanism in two-dimensional phosphorene. *Phys. Rev. B: Condens. Matter Mater. Phys.* **2014**, *90*, 085402.
(37) Singh, N.; Hua Su, C.; Arnold, B.; Choa, F.-S.; Sova, S.; Cooper, C. Multifunctional 2D- Materials: Gallium Selenide. *Materials Today: Proceedings* **2017**, *4*, 5471−5477.
(38) Phuc, H. V.; Ilyasov, V. V.; Hieu, N. N.; Amin, B.; Van der Nguyen, C. V. Waals graphene/g-GaSe heterostructure: Tuning the electronic properties and Schottky barrier by interlayer coupling, biaxial strain, and electric gating. *J. Alloys Compd.* **2018**, *750*, 765−773.
(39) Jappor, H. R.; Habeeb, M. A. Tunable electronic and optical properties of GaS/GaSe van der Waals heterostructure. *Curr. Appl. Phys.* **2018**, *18*, 673−680.
(40) Jappor, H. R. Electronic structure of novel GaS/GaSe heterostructures based on GaS and GaSe monolayers. *Phys. B* **2017**, *524*, 109−117.
(41) Jappor, H. R.; Habeeb, M. A. Optical properties of two-dimensional GaS and GaSe monolayers. *Phys. E* **2018**, *101*, 251−255.
(42) Rybkovskiy, D. V.; Osadchy, A. V.; Obraztsova, E. D. Transition from parabolic to ring-shaped valence band maximum in few-layer GaS, GaSe, and InSe. *Phys. Rev. B: Condens. Matter Mater. Phys.* **2014**, *90*, 235302.
(43) Demirci, S.; Avazlı, N.; Durgun, E.; Cahangirov, S. Structural and electronic properties of monolayer group III monochalcogenides. *Phys. Rev. B: Condens. Matter Mater. Phys.* **2017**, *95*, 115409.
(44) Chen, H.; Li, Y.; Huang, L.; Li, J. Influential Electronic and Magnetic Properties of the Gallium Sulfide Monolayer by Substitutional Doping. *J. Phys. Chem. C* **2015**, *119*, 29148−29156.
(45) Jung, C. S.; Shojaei, F.; Park, K.; Oh, J. Y.; Im, H. S.; Jang, D. M.; Park, J.; Kang, H. S. Red-to-Ultraviolet Emission Tuning of Two-Dimensional Gallium Sulfide/Selenide. *ACS Nano* **2015**, *9*, 9585−9593.
(46) Nissimagoudar, A. S.; Ma, J.; Chen, Y.; Li, W. Thermal transport in monolayer InSe. *J. Phys.: Condens. Matter* **2017**, *29*, 335702.
(47) Mudd, G. W.; Molas, M. R.; Chen, X.; Zolyomi, V.; Nogajewski, K.; Kudrynskyi, Z. R.; Kovalyuk, Z. D.; Yusa, G.; Makarovsky, O.; Eaves, L.; et al. The direct-to-indirect band gap crossover in two-dimensional van der Waals Indium Selenide crystals. *Sci. Rep.* **2016**, *6*, 39619.
(48) Ayadi, T.; Debbichi, L.; Said, M.; Lebegue, S. An *ab initio* study of the electronic structure of indium and gallium chalcogenide bilayers. *J. Chem. Phys.* **2017**, *147*, 114701.
(49) Rhyee, J.-S.; Lee, K. H.; Lee, S. M.; Cho, E.; Kim, S. I.; Lee, E.; Kwon, Y. S.; Shim, J. H.; Kotliar, G. Peierls distortion as a route to high thermoelectric performance in $In_4Se_{3-\delta}$ crystals. *Nature* **2009**, *459*, 965−968.

DOI: 10.1021/acs.jpcc.9b05681
J. Phys. Chem. C 2019, 123, 25437−25447

(50) Losovyj, Y. B.; Makinistian, L.; Albanesi, E. A.; Petukhov, A. G.; Liu, J.; Galiy, P.; Dveriy, O. R.; Dowben, P. A. The anisotropic band structure of layered In4Se3(001). *J. Appl. Phys.* **2008**, *104*, No. 083713.
(51) Hu, T.; Zhou, J.; Dong, J. Strain induced new phase and indirect−direct band gap transition of monolayer InSe. *Phys. Chem. Chem. Phys.* **2017**, *19*, 21722−21728.
(52) Bandurin, D. A.; Tyurnina, A. V.; Yu, G. L.; Mishchenko, A.; Zolyomi, V.; Morozov, S. V.; Kumar, R. K.; Gorbachev, R. V.; Kudrynskyi, Z. R.; Pezzini, S.; et al. High electron mobility, quantum Hall effect and anomalous optical response in atomically thin InSe. *Nat. Nanotechnol.* **2017**, *12*, 223−227.
(53) Boukhvalov, D. W.; Gürbulak, B.; Duman, S.; Wang, L.; Politano, A.; Caputi, L. S.; Chiarello, G.; Cupolillo, A. The Advent of Indium Selenide: Synthesis, Electronic Properties, Ambient Stability and Applications. *Nanomaterials* **2017**, *7*, 372.
(54) Petroni, E.; Lago, E.; Bellani, S.; Boukhvalov, D. W.; Politano, A.; Gürbulak, B.; Duman, S.; Prato, M.; Gentiluomo, S.; Oropesa-Nuñez, R.; et al. Liquid-Phase Exfoliated Indium-Selenide Flakes and Their Application in Hydrogen Evolution Reaction. *Small* **2018**, *14*, 1800749.
(55) Politano, A.; Chiarello, G.; Samnakay, R.; Liu, G.; Gürbulak, B.; Duman, S.; Balandin, A. A.; Boukhvalov, D. W. The influence of chemical reactivity of surface defects on ambient-stable InSe-based nanodevices. *Nanoscale* **2016**, *8*, 8474−8479.
(56) Li, Z.; Qiao, H.; Guo, Z.; Ren, X.; Huang, Z.; Qi, X.; Dhanabalan, S. C.; Ponraj, J. S.; Zhang, D.; Li, J.; et al. High-Performance Photo-Electrochemical Photodetector Based on Liquid-Exfoliated Few-Layered InSe Nanosheets with Enhanced Stability. *Adv. Funct. Mater.* **2018**, *28*, 1705237.
(57) Perdew, J. P.; Burke, K.; Ernzerhof, M. Generalized Gradient Approximation Made Simple. *Phys. Rev. Lett.* **1996**, *77*, 3865−3868.
(58) Giannozzi, P.; Andreussi, O.; Brumme, T.; Bunau, O.; Nardelli, M. B.; Calandra, M.; Car, R.; Cavazzoni, C.; Ceresoli, D.; Cococcioni, M.; et al. Advanced capabilities for materials modelling with QUANTUM ESPRESSO. *J. Phys.: Condens. Matter* **2017**, *29*, 465901.
(59) Giannozzi, P.; Baroni, S.; Bonini, N.; Calandra, M.; Car, R.; Cavazzoni, C.; Ceresoli, D.; Chiarotti, G. L.; Cococcioni, M.; Dabo, I.; et al. QUANTUM ESPRESSO: a modular and open-source software project for quantum simulations of materials. *J. Phys.: Condens. Matter* **2009**, *21*, 395502.
(60) Madsen, G. K. H.; Singh, D. J. BoltzTraP. A code for calculating band-structure dependent quantities. *Comput. Phys. Commun.* **2006**, *175*, 67−71.
(61) Li, W.; Carrete, J.; Katcho, N. A.; Mingo, N. ShengBTE: a solver of the Boltzmann transport equation for phonons. *Comput. Phys. Commun.* **2014**, *185*, 1747−1758.
(62) Hung, N. T.; Nugraha, A. R. T.; Yang, T.; Zhang, Z.; Saito, R. Thermoelectric performance of monolayer InSe improved by convergence of multivalley bands. *J. Appl. Phys.* **2019**, *125*, No. 082502.
(63) Hohenberg, P.; Kohn, W. Inhomogeneous Electron Gas. *Phys. Rev.* **1964**, *136*, B864−B871.
(64) Kohn, W.; Sham, L. J. Self-Consistent Equations Including Exchange and Correlation Effects. *Phys. Rev.* **1965**, *140*, A1133−A1138.
(65) Garrity, K. F.; Bennett, J. W.; Rabe, K. M.; Vanderbilt, D. Pseudopotentials for high-throughput DFT calculations. *Comput. Mater. Sci.* **2014**, *81*, 446−452.
(66) Methfessel, M.; Paxton, A. T. High-precision sampling for Brillouin-zone integration in metals. *Phys. Rev. B: Condens. Matter Mater. Phys.* **1989**, *40*, 3616−3621.
(67) Bardeen, J.; Shockley, W. Deformation Potentials and Mobilities in Non-Polar Crystals. *Phys. Rev.* **1950**, *80*, 72−80.
(68) Xi, J.; Long, M.; Tang, L.; Wang, D.; Shuai, Z. First-principles prediction of charge mobility in carbon and organic nanomaterials. *Nanoscale* **2012**, *4*, 4348−4369.
(69) Price, P. J. Two-dimensional electron transport in semiconductor layers. *Ann. Phys.* **1981**, *133*, 217−239.
(70) Li, W.; Mingo, N.; Lindsay, L.; Broido, D. A.; Stewart, D. A.; Katcho, N. A. Thermal conductivity of diamond nanowires from first principles. *Phys. Rev. B: Condens. Matter Mater. Phys.* **2012**, *85*, 195436.
(71) Li, W.; Lindsay, L.; Broido, D. A.; Stewart, D. A.; Mingo, N. Thermal conductivity of bulk and nanowire Mg_2 Si_x Sn_{1-x} alloys from first principles. *Phys. Rev. B: Condens. Matter Mater. Phys.* **2012**, *86*, 174307.
(72) Zolyomi, V.; Drummond, N. D.; Fal'ko, V. I. Electrons and phonons in single layers of hexagonal indium chalcogenides from ab initio calculations. *Phys. Rev. B: Condens. Matter Mater. Phys.* **2014**, *89*, 205416.
(73) Sun, Y.; Luo, S.; Zhao, X.-G.; Biswas, K.; Li, S.-L.; Zhang, L. InSe: a two-dimensional material with strong interlayer coupling. *Nanoscale* **2018**, *10*, 7991−7998.
(74) Cooper, R. C.; Lee, C.; Marianetti, C. A.; Wei, X.; Hone, J.; Kysar, J. W. Nonlinear elastic behavior of two-dimensional molybdenum disulfide. *Phys. Rev. B: Condens. Matter Mater. Phys.* **2013**, *87*, No. 035423.
(75) Politano, A.; Chiarello, G. Probing the Young's modulus and Poisson's ratio in graphene/metal interfaces and graphite: a comparative study. *Nano Res.* **2015**, *8*, 1847−1856.
(76) Pandey, T.; Parker, D. S.; Lindsay, L. Ab initio phonon thermal transport in monolayer InSe, GaSe, GaS, and alloys. *Nanotechnology* **2017**, *28*, 455706.
(77) Pei, Y.; Shi, X.; LaLonde, A.; Wang, H.; Chen, L.; Snyder, G. J. Convergence of electronic bands for high performance bulk thermoelectrics. *Nature* **2011**, *473*, 66−69.
(78) Liu, W.; Tan, X.; Yin, K.; Liu, H.; Tang, X.; Shi, J.; Zhang, Q.; Uher, C. Convergence of Conduction Bands as a Means of Enhancing Thermoelectric Performance of n-Type $Mg_2Si_{1-x}Sn_x$ Solid Solutions. *Phys. Rev. Lett.* **2012**, *108*, 166601.
(79) Tan, X. J.; Liu, W.; Liu, H. J.; Shi, J.; Tang, X. F.; Uher, C. Multiscale calculations of thermoelectric properties of n-type $Mg_2Si_{1-x}Sn_x$ solid solutions. *Phys. Rev. B: Condens. Matter Mater. Phys.* **2012**, *85*, 205212.
(80) Hung, N. T.; Nugraha, A. R. T.; Saito, R. Two-dimensional InSe as a potential thermoelectric material. *Appl. Phys. Lett.* **2017**, *111*, No. 092107.
(81) Zhao, L.-D.; He, J.; Berardan, D.; Lin, Y.; Li, J.-F.; Nan, C.-W.; Dragoe, N. BiCuSeO oxyselenides: new promising thermoelectric materials. *Energy Environ. Sci.* **2014**, *7*, 2900−2924.
(82) He, Y.; Day, T.; Zhang, T.; Liu, H.; Shi, X.; Chen, L.; Snyder, G. J. High Thermoelectric Performance in Non-Toxic Earth-Abundant Copper Sulfide. *Adv. Mater.* **2014**, *26*, 3974−3978.
(83) Anderson, C. Selenium and Tellurium Statistics and Information, 2019. www.usgs.gov/centers/nmic/selenium-and-tellurium-statistics-and-information.
(84) Sowjanya, V.; Bangera, K. V.; G K, S. Synthesis of single-phase stoichiometric InTe thin films for opto-electronic applications. *Superlattices Microstruct.* **2019**, *129*, 220−225.
(85) Bahuguna, B. P.; Saini, L. K.; Sharma, R. O.; Tiwari, B. Hybrid functional calculations of electronic and thermoelectric properties of GaS, GaSe, and GaTe monolayers. *Phys. Chem. Chem. Phys.* **2018**, *20*, 28575−28582.
(86) Shangguan, H.; Han, L.; Zhang, T.; Quhe, R.; Wang, Q.; Li, S.; Lu, P. Thermoelectric Properties of Two-Dimensional Gallium Telluride. *J. Electron. Mater.* **2019**, *48*, 5988−5994.
(87) Vega-Flick, A.; Jung, D.; Yue, S.; Bowers, J. E.; Liao, B. Reduced thermal conductivity of epitaxial GaAs on Si due to symmetry-breaking biaxial strain. *Physical Review Materials* **2019**, *3*, 034603.
(88) Meng, X.; Pandey, T.; Jeong, J.; Fu, S.; Yang, J.; Chen, K.; Singh, A.; He, F.; Xu, X.; Zhou, J.; et al. Thermal Conductivity Enhancement in MoS_2 under Extreme Strain. *Phys. Rev. Lett.* **2019**, *122*, 155901.
(89) Zhou, J.; Shi, J.; Zeng, Q.; Chen, Y.; Niu, L.; Liu, F.; Yu, T.; Suenaga, K.; Liu, X.; Lin, J.; et al. InSe monolayer: synthesis, structure and ultra-high second-harmonic generation. *2D Mater.* **2018**, *5*, No. 025019.

DOI: 10.1021/acs.jpcc.9b05681
J. Phys. Chem. C 2019, 123, 25437−25447

(90) Frank, O.; Mohr, M.; Maultzsch, J.; Thomsen, C.; Riaz, I.; Jalil, R.; Novoselov, K. S.; Tsoukleri, G.; Parthenios, J.; Papagelis, K.; et al. Raman 2D-Band Splitting in Graphene: Theory and Experiment. *ACS Nano* **2011**, *5*, 2231−2239.
(91) Huang, M.; Yan, H.; Chen, C.; Song, D.; Heinz, T. F.; Hone, J. Phonon softening and crystallographic orientation of strained graphene studied by Raman spectroscopy. *Proc. Natl. Acad. Sci. U. S. A.* **2009**, *106*, 7304−7308.
(92) Polyzos, I.; Bianchi, M.; Rizzi, L.; Koukaras, E. N.; Parthenios, J.; Papagelis, K.; Sordan, R.; Galiotis, C. Suspended monolayer graphene under true uniaxial deformation. *Nanoscale* **2015**, *7*, 13033−13042.

DOI: 10.1021/acs.jpcc.9b05681
J. Phys. Chem. C 2019, 123, 25437−25447